Examining the Performance of Implantable-Grade Lithium-Ion Cells after Overdischarge and Thermally Accelerated Aging

Jonathon R. Harding *, Binghong Han, Samuel B. Madden and Quinn C. Horn *

Exponent, Inc., 1075 Worcester St., Natick, MA 01760, USA; bhan@exponent.com (B.H.);
smadden@exponent.com (S.B.M.)
* Correspondence: jharding@exponent.com (J.R.H.); qhorn@exponent.com (Q.C.H.)

Abstract: For implanted medical devices containing rechargeable batteries, maximizing battery life-time is paramount as surgery is required for battery replacement. In non-life-sustaining applications (e.g., spinal cord stimulators or sacral nerve modulation), these implants may be left unused and unmaintained for extended periods, according to patient preference or in the case of unexpected life events. In this study, we examine the performance of two commercial lithium-ion cells intended for implantable neurostimulators (using lithium titanium oxide (LTO) and graphite as the negative electrode) when subjected to repeated deep overdischarge and to aging at a high state of charge (SOC). The graphite-based cells exhibited significant performance decline and swelling after overdischarge and became unable to store a charge after 42 days at 0 V. In contrast, the LTO-based cells exhibited minimal changes in performance even after 84 days (the length of the study) at 0 V. When subjected to an accelerated aging protocol at 100% SOC, the graphite-based cells were found to age more rapidly than the LTO cells, which exhibited minimal aging over the course of the study period. These results show that practical LTO-based lithium-ion cells are much more tolerant of abuse as a result of neglect and misuse and are worth considering for use in high-value applications where battery replacement is difficult or impossible.

Keywords: implantable batteries; lithium titanium oxide; overdischarge; accelerated aging; spinal cord stimulation; sacral nerve stimulation

1. Introduction

Rechargeable batteries for use in implanted medical devices face a unique set of constraints not encountered in most other applications. The human body temperature is 37 °C, which will cause the accelerated aging of any lithium-ion battery (relative to room temperature). In addition, cell lifetime is paramount, as surgery is required to replace any defective or damaged batteries. This puts greater stress on designing cells that are exceptionally long-lived. Particularly in the case of non-life-saving applications, there is a significant likelihood that a patient may elect to leave a device unused for extended periods of time without maintaining or removing it. Therefore, cells need to tolerate potential extended storage at a high state of charge (SOC) as well as at a very low SOC (or even under overdischarge conditions).

Medtronic has recently developed a line of implantable batteries that use lithium titanium oxide (LTO) as the negative electrode, in place of the graphite electrode used in traditional lithium-ion cells. LTO is well-known to be more stable than graphite, as the LTO surface is stable in most non-aqueous electrolytes. Although early reports suggested that LTO did not form an solid electrolyte interphase (SEI) layer (due to its high operating potential), recent studies have shown that an SEI layer builds up on LTO-based negative electrodes [1,2]. Other work has explored the response of LTO electrodes to extended overdischarge [3]. However, few studies have investigated the long-term performance of this category of cells when subjected to implant-like conditions.

In this work, we compare the performance of Medtronic's LTO-based lithium-ion batteries against implantable-grade graphite-based cells manufactured by a third party. We explore the responses of both types of cells to repeated deep overdischarge (7-day-long holds at 0 V) to examine how these cells might respond to extended periods without being recharged. We also conduct tests on the thermally accelerated aging of cells held at high states of charge, which are then used to develop predictive aging models based on the Arrhenius equation to estimate the long-term performance of cells stored at high states of charge.

Our results indicate that LTO-based cells can be much more stable than graphite-based cells against extended aging at both a high SOC and in overdischarge conditions. These findings can help guide the selection and development of more stable lithium-ion cells for medical devices and other applications that may require the cells to tolerate extended periods of storage.

2. Materials and Methods

2.1. Cells Tested

Medtronic provided twenty-five lithium titanium oxide (LTO)-based cells (manufactured by Medtronic) and ten graphite-based lithium-ion cells (manufactured by a third party, a leading implantable cell manufacturer). All cells were intended for use in implanted sacral neurostimulation stimulation devices. The LTO-based cells used lithium cobalt oxide (LCO) for the positive electrode active material, with a normal operating voltage window of 1.8 V to 2.8 V. The graphite-based cells used lithium nickel cobalt aluminum (NCA) for the positive electrode active material with an operating window of 3.0 V to 4.1 V. Within each population, cells were divided into three different test groups: baseline cycling (5 LTO, 2 graphite), overdischarge cycling (5 LTO, 2 graphite), and accelerated aging (15 LTO, 6 graphite).

2.2. Baseline Cycling

Cells subjected to baseline cycling were kept in a 37 °C test chamber and cycled using the following parameters: a charge at the cell's manufacturer's recommended charge rate, using a constant-current (CC) charging rate (LTO: 2.5C; graphite: 0.5C) to the cell manufacturer's specification and recommendation maximum voltage (LTO: 2.8 V; graphite: 4.1 V), with a constant voltage (CV) hold sustained at that voltage until the current fell below 0.1C. Cells were then allowed to rest at an open circuit for 30 min, before being discharged at a constant current rate of 0.5C to the minimum operating voltage (LTO: 1.8 V; graphite: 3.0 V). Cells were again rested for 30 min prior to recharge. On a periodic basis (described below), two characterization discharges were performed: a CC discharge at a rate of C/24 (0.04166̄C; "C/24 discharge"), and a CC discharge at 0.5C with a 10-min rest at open circuit every 12 min ("DC internal resistance (DCIR) discharge"). The same charge protocol was used for all cycles. The C/24 discharge cycles were performed on cycle numbers 2, 52, 102, 202, . . . , and the DCIR discharge cycles were performed on cycle numbers 3, 53, 103, 203, ... Baseline cycling continued indefinitely and continued for the duration of the study.

2.3. Overdischarge Cycling

Cells subjected to overdischarge cycling were kept in a 37 °C test chamber and were cycled using a modified version of the baseline cycling protocol described in Section 2.2 above. During selected overdischarge cycles, the cells were first discharged normally and allowed to rest for 30 min. After this, they were subjected to a CV hold maintained at the lower operating voltage until the current fell below 0.01C. Each cell was then discharged at constant current, at 0.01C to 0 V, and then held at 0 V for 168 h (7 days). Following this, the cells were recharged at a 0.1C constant current rate at the lower operating voltage limit. Cycling was suspended at this point, to allow for thickness measurement, before resuming.

Overdischarge cycles were performed at the end of cycles 50, 100, 150, 200, ... The C/24 and DCIR discharge cycles were performed using the same schedule as for the baseline cycling protocol.

After 400 cycles (8 weeks in total at 0 V), the cycling protocol was modified for the remaining (LTO) cells, to extend each overdischarge period to last for 4 weeks (672 h), in order to accelerate the aging process. In addition, the C/24 and DCIR discharge cycles were included after every overdischarge period (rather than after every 100 cycles).

Graphite cells were removed from testing when they were no longer capable of storing a charge. LTO cells were subjected to 10 overdischarge periods (500 cycles) for a total of 112 days at 0 V.

2.4. Thermally Accelerated Aging

For the accelerated aging study, cells were divided evenly into three groups for aging at 45 °C, 50 °C, and 55 °C. Prior to aging and approximately every two weeks thereafter, all test chambers were set to 37 °C, and cells were subjected to a characterization protocol consisting of an initial constant current discharge at 0.5C, a standard discharge cycle, a C/24 discharge cycle, and a DCIR discharge cycle (following the conditions specified in Section 2.2). Cells were then fully charged, after which the chamber temperatures were raised to the experimental set point and the aging protocol was initiated.

During aging, each cell's voltage was continuously monitored. If the cell voltage fell below the voltage estimated to reflect 95% SOC (LTO: 2.47 V; graphite: 4.03 V), then the cell was recharged. Cells were allowed to rest indefinitely between recharges.

The recharge voltage limits were determined using an open-circuit voltage (OCV) determination cycle, in which cells were charged and then discharged at a constant current rate of 0.1C. All cells undergoing aging were subjected to this cycle, prior to the first characterization measurements. The cell recharge voltage was selected to be consistent with an SOC of 95% for that population.

2.5. Cell Cross-Sectioning

Selected cells were cross-sectioned after the completion of testing. Cross-sectioning was performed by puncturing the cell can, soaking the cell in dimethyl carbonate, then filling the cell with metallographic epoxy. Once cured, the cells were cut with a bandsaw and backfilled with additional epoxy; a water-free polish was then applied and the cells were optically imaged. The samples were then ion polished and imaged with a scanning electron microscope.

2.6. Equipment Used

All charge/discharge testing was performed using a Maccor 4000 battery cycler (current accuracy 0.03 mA during cycling, 0.03 µA during overdischarge; voltage accuracy 2 mV). Cell thickness measurements were performed using a flat anvil thickness gauge (resolution 0.01 mm, accuracy ± 0.025 mm, model 547-520S, Mitutoyo America Corporation, Aurora, IL, USA). Cells tested at 37 °C, 45 °C, and 50 °C were tested in benchtop incubators (Heratherm General Protocol Microbiological catalog number 51028063, ThermoFisher Scientific, Waltham, MA, USA), temperature uniformity ± 0.6 °C, temperature stability ± 0.2 °C). Cells tested at 55 °C were tested in a benchtop oven (±0.3 °C accuracy, ±1.0 °C uniformity, model Symphony 414004-564, VWR International, Radnor, PA, USA). Cross-sections were imaged using an optical microscope (Model UC50, Olympus Scientific, Tokyo, Japan). Ion polishing was performed using an ion-beam polisher (JEOL USA, Peabody, MA, USA). Scanning electron microscopy (SEM) imaging and energy-dispersive X-ray spectroscopy (EDS) maps were collected with a JEOL JSM-IT800 SEM (JEOL USA, Peabody, MA, USA). EDS spectra were acquired with a JEOL JSM-6390LV scanning electron microscope (JEOL USA, Peabody, MA, USA).

3. Results

3.1. Baseline Cycling

Five LTO and two graphite cells were cycled under the baseline cycling protocol detailed above at 37 °C. Figure 1 shows the normalized discharge capacity and DCIR at 50% of the rated SOC for these cells. The method used for calculating DCIR is described in Appendix A. The data in Figure 1 represent approximately 254 days of active cycling for the graphite cells and approximately 260 days of active cycling for the LTO cells; the difference in the total number of cycles achieved reflects the faster charge rate used for LTO cells.
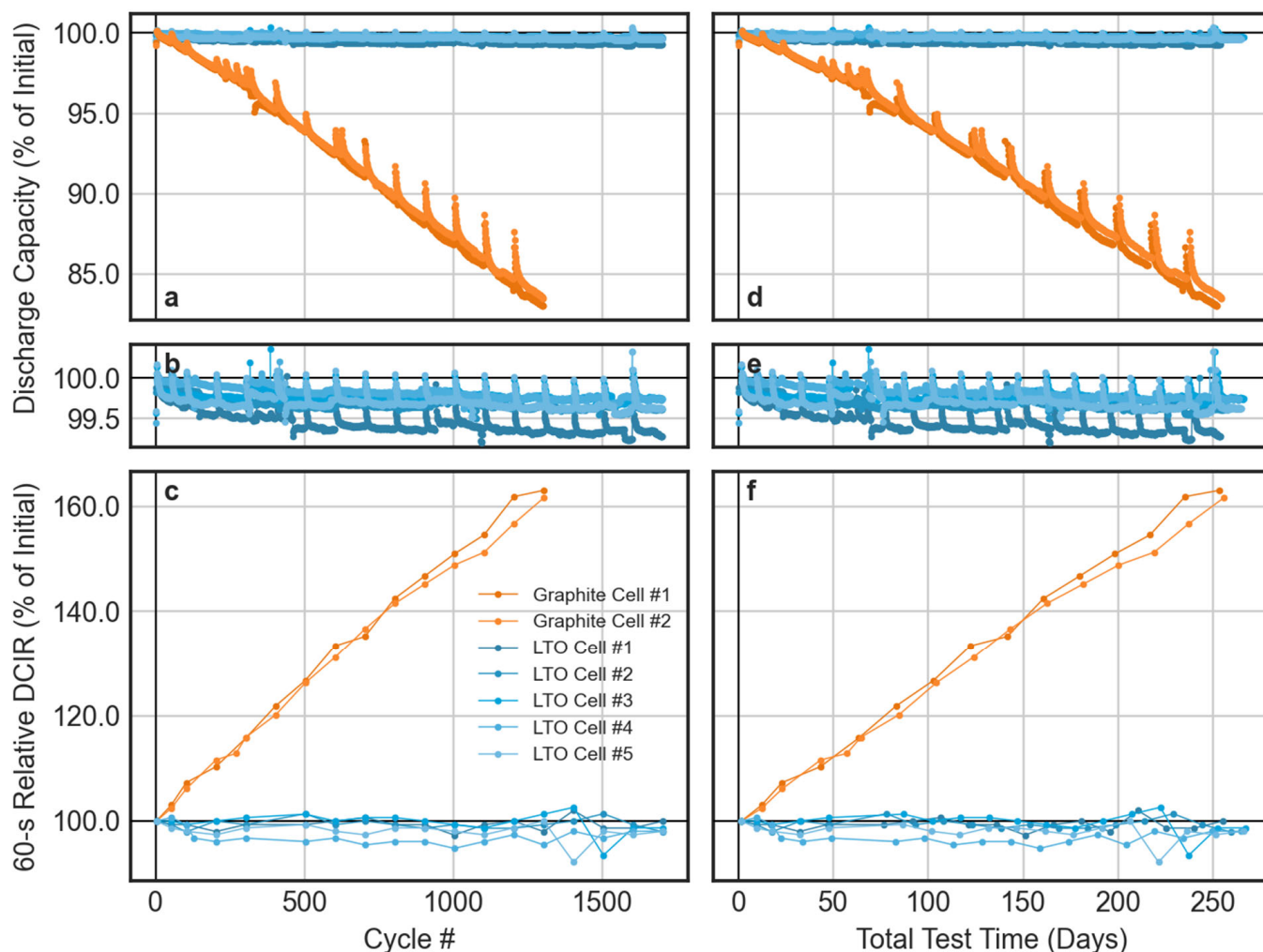
Figure 1. The left-hand column shows the standard cycle discharge capacity (**a,b**) and DC internal resistance (DCIR) at 50% depth-of-discharge (DoD) (**c**), vs. the number of cycles for baseline cells. The right-hand column (**d–f**) shows the same metrics presented against total active testing time. All cycles were performed at 37 ± 1 °C. Orange colors indicate graphite cells; blue colors indicate lithium titanium oxide (LTO) cells.

The LTO cells retained more than 99.5% of their original capacity after 1600 cycles (more than 8 months) of continuous cycling at 37 °C. No significant change in the DCIR at 50% of the rated depth-of-discharge (DoD) was observed for these cells over this period. After 1000 cycles at 37 °C, the graphite cells had approximately 87% of their rated capacity, which agrees well with the manufacturer's specification sheet for these cells (88% of the rated capacity after 1000 cycles at 37 °C and C/2). They also exhibit an increase of about 50% in DCIR at 50% DoD.

Both cells continued to follow an approximately linear trend on both metrics, consistent with cells that are not yet at their end-of-life [4–6]. The capacity loss and growth in DCIR

that were observed in the graphite cells were as expected for a traditional lithium-ion cell, where SEI growth over time (especially at high states of charge) is expected to consume the lithium (leading to capacity loss) and increase the charge transfer resistance at the negative electrode (increasing cell internal resistance and further decreasing capacity) [7,8].

Both the LTO and graphite cells exhibited significant capacity hysteresis following each characterization period, showing an elevated discharge capacity for several cycles following each C/24 discharge cycle. For the LTO cells, 19.8 cycles were required on average before the cell's discharge capacity fell to the level it had been at prior to each C/24 discharge. The graphite cells required 13.4 cycles on average to reach the same level. Investigating the cause of this phenomenon is outside the scope of this study, but it can be attributed to the formation of stable lithium concentration gradients within larger particles in one or both electrodes during high-rate cycling [9]. The C/24 discharge cycles effectively disrupt these concentration gradients, as more time is provided for the lithium to diffuse within the electrodes' active material particles at the end of discharge. We note that this effect is an artifact of the accelerated cycling regime; practical applications for these cells will use slow discharges (over the course of days) and would not develop the proposed concentration gradients.

The differential capacity (dQ/dV) profiles in Figure 2 show that little had changed in the discharge profile of the LTO cells between cycle 1402 and cycle 2. The method for calculating differential capacity is described in Appendix B. All cells showed a dominant peak at 2.327–2.329 V, reflecting the primary plateau for the intercalation of lithium into the lithium cobalt oxide positive electrode, used in these cells, and the flat voltage profile of LTO [10]. The graphite cells did not exhibit a single primary discharge plateau, even when new, which is consistent with the complex dQ/dV profile of NCA/graphite cells [11]. After 1200 cycles, these cells showed a slight downward shift in peak positions (reflecting the impact of elevated internal resistance) and a reduction in peak intensity, especially at lower voltages, which is consistent with other studies of NCA/graphite cells after extended cycling [11].

3.2. Overdischarge Cycling

Figure 3 shows the results for five LTO and two graphite cells that were subjected to repeated overdischarge to 0 V. Every 50 cycles, each cell was discharged to 0 V and maintained under a constant voltage (CV) hold at 0 V for 7 days. The graphite cells were removed from cycling after six overdischarge periods (42 days at 0 V). After eight overdischarge periods (56 days at 0 V), the test protocol was altered to expose the LTO cells to 4-week-long 0 V holds, in order to accelerate the rate of aging. This study design (repeated overdischarge of individual cells) was chosen to maximize the research value of the limited number of cells available, by measuring the response of a small number of cells to overdischarge conditions over time.

After each overdischarge period, the graphite cells exhibited a short-lived (~10 cycle) and rapid loss of capacity, after which the rate of capacity loss per cycle declined (although it remained significant throughout each 50-cycle period). The rate of capacity loss also accelerated after each overdischarge period, as shown in Figure 3, with each overdischarge period resulting in a progressively larger capacity loss. Following the sixth overdischarge period (42 days at 0 V), the graphite cells were incapable of storing a charge above 3.0 V, after which they were removed from cycling. After nine overdischarge periods (84 days at 0 V), the LTO cells continued to exhibit nearly unchanged discharge capacities (>99% of their original capacity). These cells exhibited a similar hysteresis response, with a small capacity increase for several cycles after each overdischarge, like the one observed for both cell types following the C/24 discharge during baseline cycling.
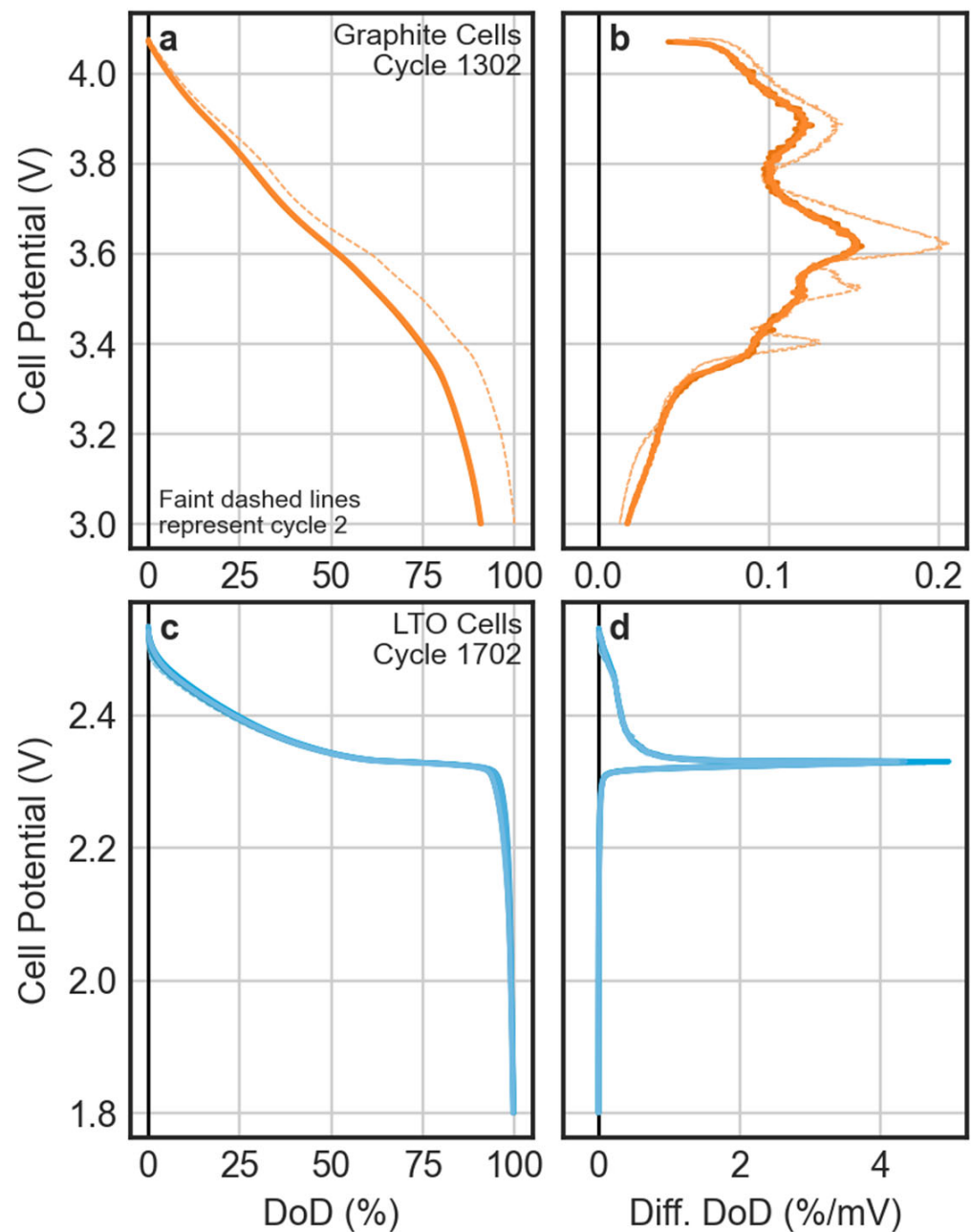
Figure 2. Cell potential vs. depth-of-discharge (DoD; (**a**,**c**)) and differential DoD (**b**,**d**) for the graphite (**a**,**b**) and lithium titanium oxide (LTO) (**c**,**d**) cells, during selected C/24 discharges. DoDs are normalized to the initial C/24 discharge capacity for each cell. The differential capacity plots include faint dashed lines that show the initial cycle performance. These are covered by other lines on the LTO differential capacity plot.

Figure 2d shows the relative change in DCIR at 20% of the rated DoD for both cell types, after spending an increasing period of time at 0 V. A value of DCIR at 20% DoD is used here because the graphite cells lost more than 50% of their capacity before the DCIR measurement was performed at cycle 203. This shows that the graphite cells experienced accelerating growth in DCIR with the passage of time at 0 V, which is consistent with repeated degradation of the SEI and consumption of the electrolyte. Slight (< 10%) changes in DCIR were observed for the LTO cells after a total of 84 days at 0 V.

Figure 2e shows the relative change in battery cell thickness with the passage of time at 0 V. Both cells had a hard metal case with two flat faces that limited the cells' ability to

swell. The graphite cells exhibited accelerating swelling (up to a maximum of 14%) after each overdischarge, which was likely due to the production of significant quantities of gas during each subsequent recharge. No measurable swelling was observed on the LTO cells. No evidence of electrolyte leakage or other indications of the cell case being compromised were observed in either cell type, even after the graphite cells no longer functioned.
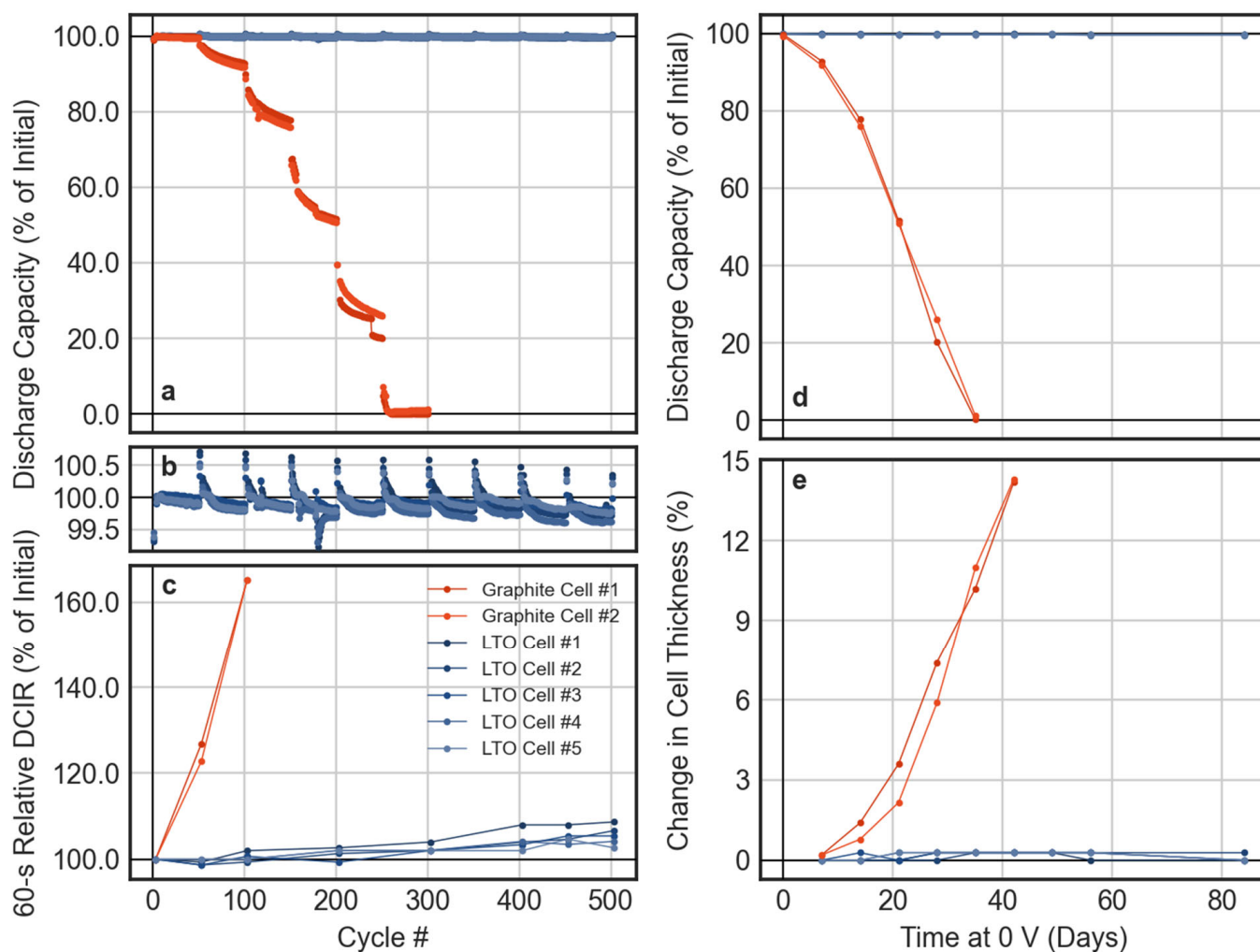

Figure 3. Overdischarge cycling performance data. The left-hand column shows the standard cycle discharge capacity (**a,b**) and DCIR @ 50% SOC (**c**) vs. the number of cycles for overdischarged cells. Right-hand column: (**d**) the final discharge capacity prior to each overdischarge and (**e**) DCIR @ 50% SOC vs. total time spent at 0 V.

The C/24 discharge profile and differential capacity plot for selected cycles for both cell types are shown in Figure 4. In the C/24 discharge following the first overdischarge period, some loss of peak resolution was apparent in the graphite cells, but the largest peak at 3.6 V remains prominent. After 14 days at 0 V, this peak has been largely eliminated, resulting in a nearly linear discharge profile for most of the discharge. The LTO cells exhibited a single large discharge plateau around 2.326–2.330 V throughout cycling without a change, which is consistent with the cell's behavior during baseline cycling. A very slight increase in the differential capacity was seen at the start of discharge relative to the uncycled cell; we attribute this as being another manifestation of the excess capacity observed in these cells, following a deep discharge.
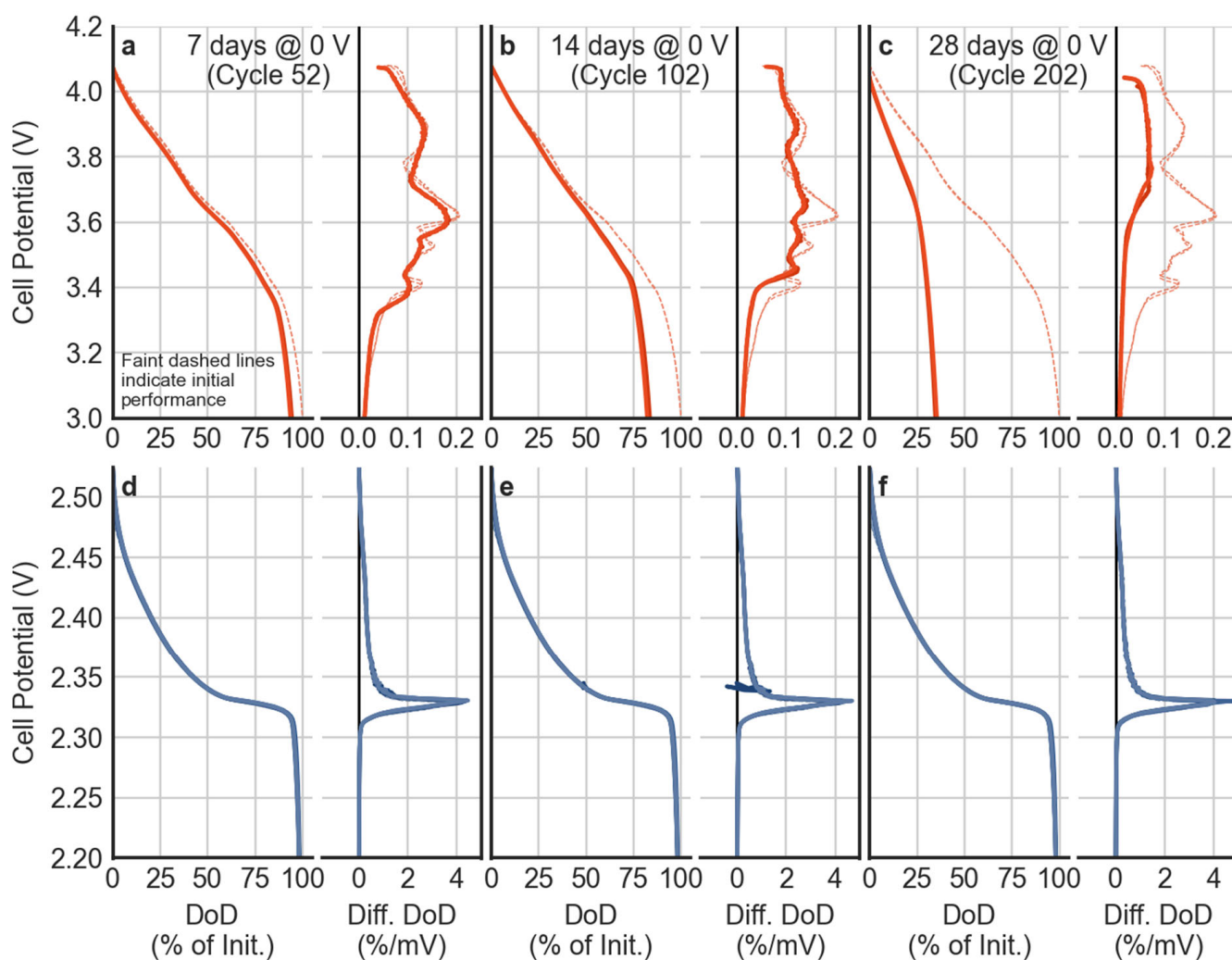
Figure 4. Differential capacity plots for selected C/24 discharge cycles, following different overdischarge regimes. Faint dashed lines represent the initial C/24 discharge performance for each cell. Top row (**a**–**c**): graphite cells. Bottom row (**d**–**f**): LTO cells. Left column (**a**,**d**): performance after 7 days at 0 V. Middle column (**b**,**e**): performance after 14 days at 0 V. Right column (**c**,**f**): performance after 28 days at 0 V. Each column shows the cell potential vs. DoD(**left**) and differential DoD (**right**). DoDs are normalized to the initial C/24 discharge capacity for each cell. LTO voltage data below 2.2 V is not shown. Plots include faint dashed lines, which show the performance during cycle 2. These are covered by other lines for the LTO cells at all cycle counts.

Figure 5 presents the charge extracted from each cell during each overdischarge period. Both cell types exhibited an initial decay in the current passed during the first several hours (as the cell relaxes from the C/100 discharge and approaches a steady state). During the first overdischarge period, the graphite cells passed 7.0% to 8.0% of their rated capacity during the CV hold at 0 V (see Figure 6). During the second overdischarge, this decreased from 6.5% to 6.8%, after which the amount of charge passed increased with each successive overdischarge period. The LTO cells passed a much smaller fraction of their rated capacity during the first overdischarge period (1.1–1.3%), which declined during the second overdischarge period (0.7–0.9%). Subsequent overdischarge periods behaved similarly, with only a very slight change in accumulated charge (0.8–1.0% of rated capacity) by the 8th week of overdischarge.
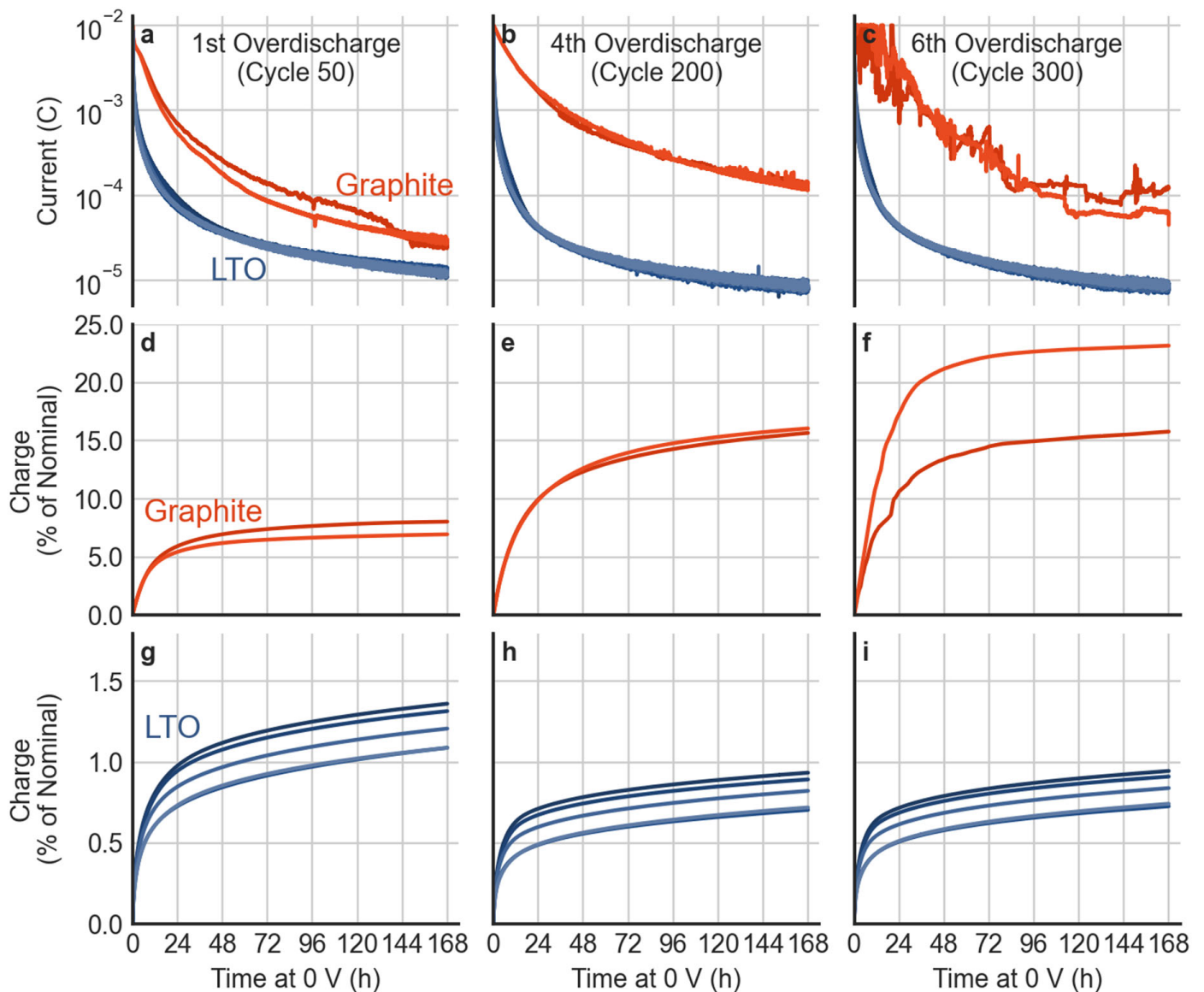
Figure 5. Current (**a**–**c**) and charge (**d**–**i**) vs. time for selected 0 V holds. The top row shows both graphite (red) and LTO (blue) cells. The charges passed for graphite (**middle row**) and LTO (**bottom row**) are presented separately. The left column (**a**,**d**,**g**) shows the first overdischarge. The middle column (**b**,**e**,**h**) shows the fourth overdischarge, and the right column (**c**,**f**,**i**) shows the sixth overdischarge.

3.3. Cross-Sectioning of Tested Cells

After testing, four cells were selected for metallurgical cross-sections: one of each type after overdischarge testing, and one of each type after aging at 45 °C. Optical microscopy (OM; Figure 7) and scanning electron microscopy (SEM; Figure 8) were used to collect images.
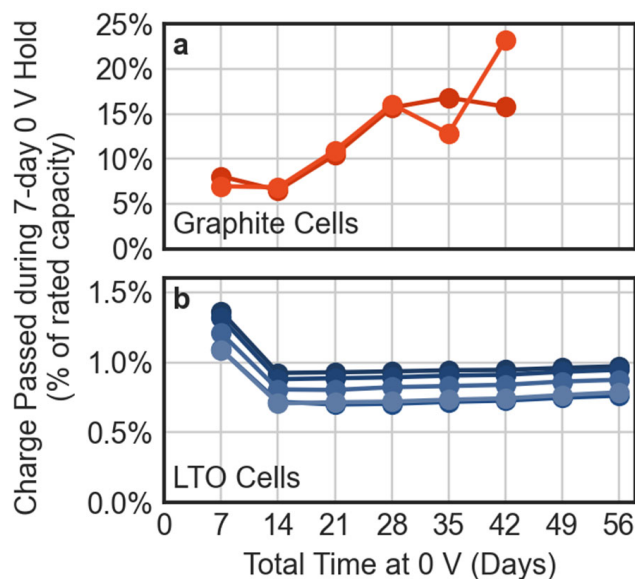
Figure 6. Total charge passed by each cell during each 7-day hold at 0 V. Graphite (**a**) and LTO (**b**) cells are presented separately.
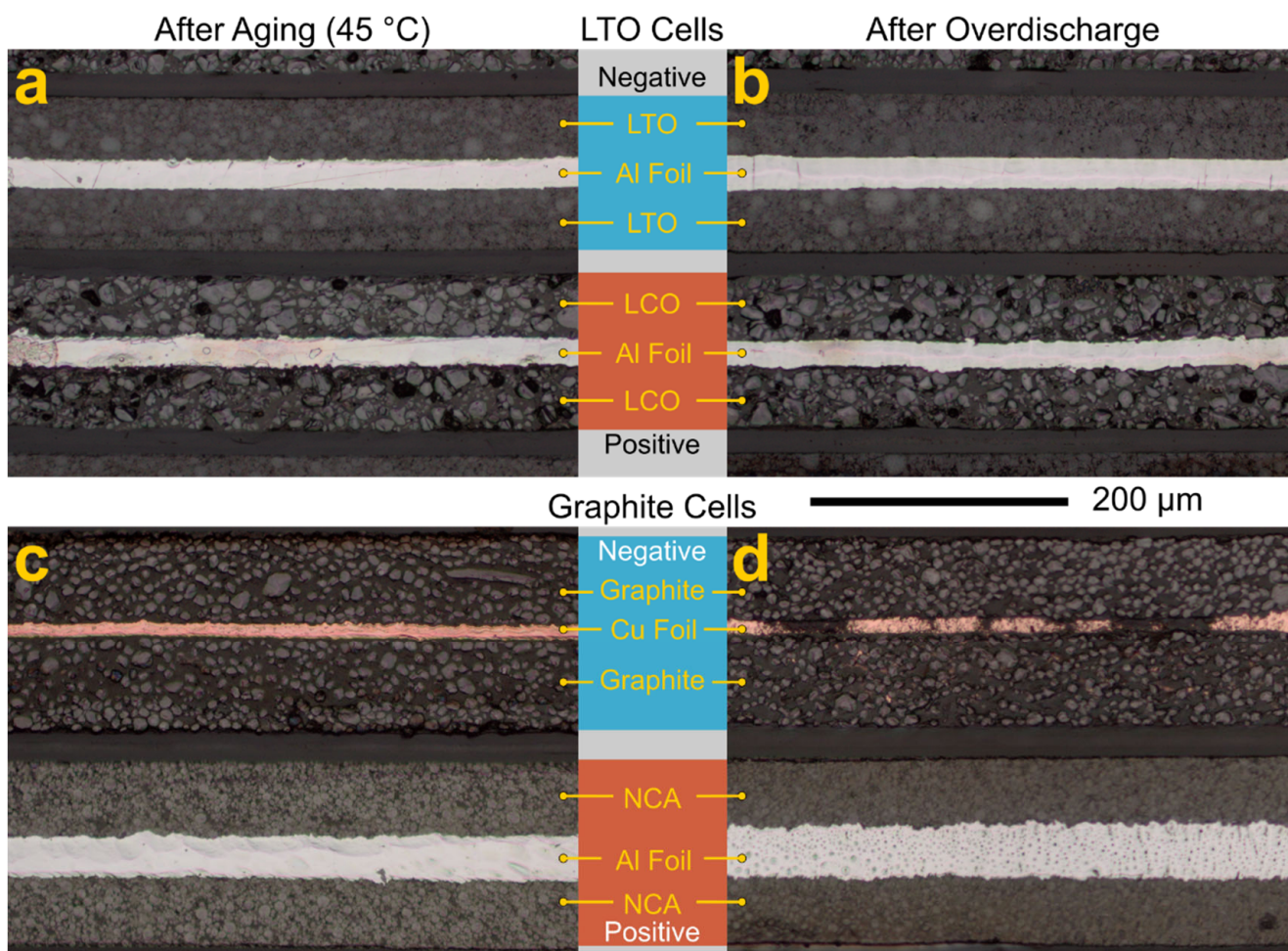
Figure 7. Optical microscopy of cross-sectioned LTO (**top row**) and graphite (**bottom row**) cells. (**a**) An LTO cell, after aging at 45 °C; (**b**) an LTO cell after overdischarge testing; (**c**) a graphite cell after aging at 45 °C; (**d**) a graphite cell after overdischarge testing. Images are oriented so that the negative electrode is above the positive electrode. All images are scaled equally.
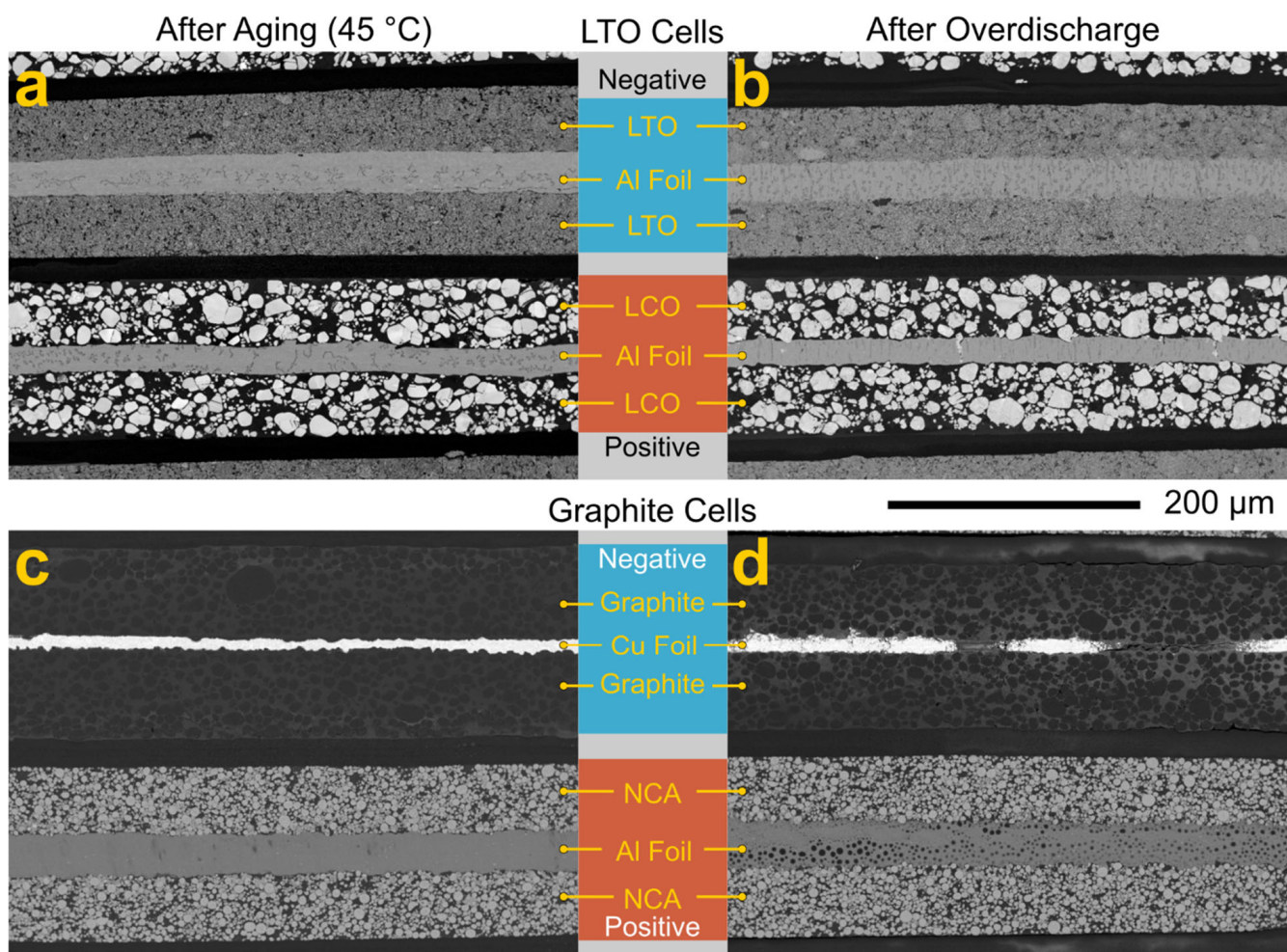
Figure 8. Backscatter electron micrographs of electrodes from the cross-sectioned LTO (**top row**) and graphite (**bottom row**) cells. (**a**) An LTO cell after aging at 45 °C; (**b**) an LTO cell after overdischarge testing; (**c**) a graphite cell after aging at 45 °C; (**d**) a graphite cell after overdischarge testing. The images here are representative and do not correspond to the specific locations shown in Figure 7. The images were collected with a 3 keV electron beam. All images are scaled equally.

Evidence of the dissolution of the copper current collector is apparent throughout the overdischarged graphite cell. Additional copper was visible in both OM and SEM (as bright deposits) within the negative electrode of this cell, which is a result of the spontaneous redeposition of copper during subsequent charges. Energy-dispersive X-ray spectroscopy (EDS) was also performed on each electrode (see Figure 9). These spectra show that the LTO cells use lithium titanium oxide as the negative electrode and lithium cobalt oxide as the positive electrode (lithium is not detected in these EDS results). The graphite cells use graphite in the negative electrode (with no discernable additives), and lithium nickel cobalt aluminum oxide (NCA) in the positive electrode.

Copper was present in the EDS spectra of the graphite negative electrode after overdischarge, as shown in Figure 9, even though the collection area did not include the current collector. This is consistent with the signs of copper in the OM and SEM micrographs. Figure 10 shows an EDS map of the copper signal in the graphite cells; low-intensity copper signals are visible in several regions of the overdischarged cell's negative electrode, in addition to the regions where the current collector was completely dissolved. The map of the aged graphite cell shows no detectable Cu signal in the negative electrode outside of the current collector.
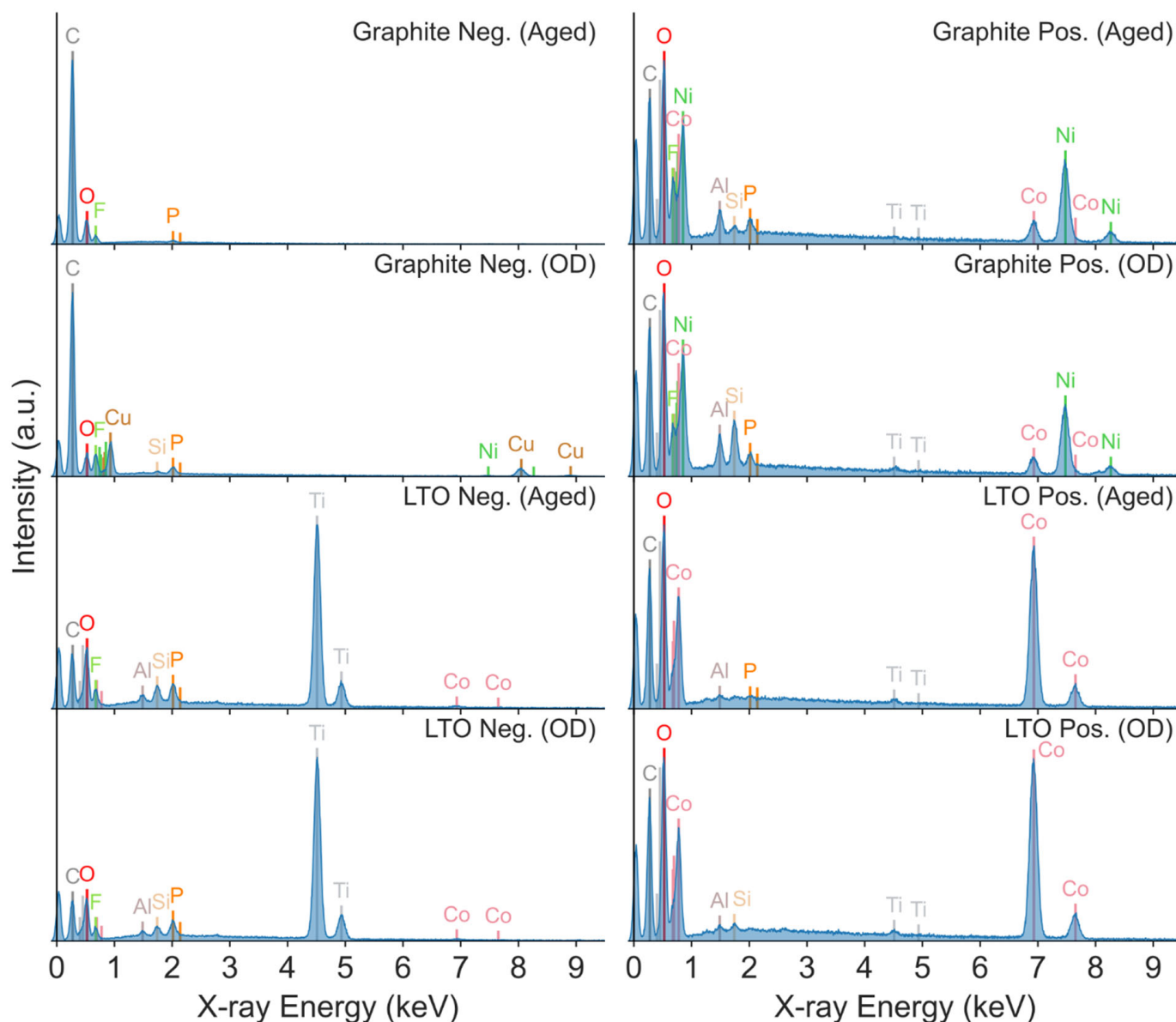
Figure 9. Energy-dispersive X-ray spectroscopy (EDS) spectra of the cross-sectioned electrodes. The left column shows the negative electrode spectra; the right column shows the positive electrode spectra. Top row: a graphite cell after aging at 45 °C. Second row: a graphite cell after overdischarge testing. Third row: an LTO cell after aging at 45 °C. Bottom row: an LTO cell after overdischarge testing. All spectra are normalized to the maximum peak height. Atomic X-ray lines are marked and colored using the Jmol color scheme [12].

Phosphorous and fluorine can be attributed to the residual electrolytes present in the cells. Silicon can be attributed to residues from the grinding media (silicon carbide). Trace titanium in the positive electrode of the LTO cells can be attributed to contamination from the negative electrode during polishing. The aluminum in both LTO cell electrodes and the graphite cell's positive electrode can be attributed to the current collector.
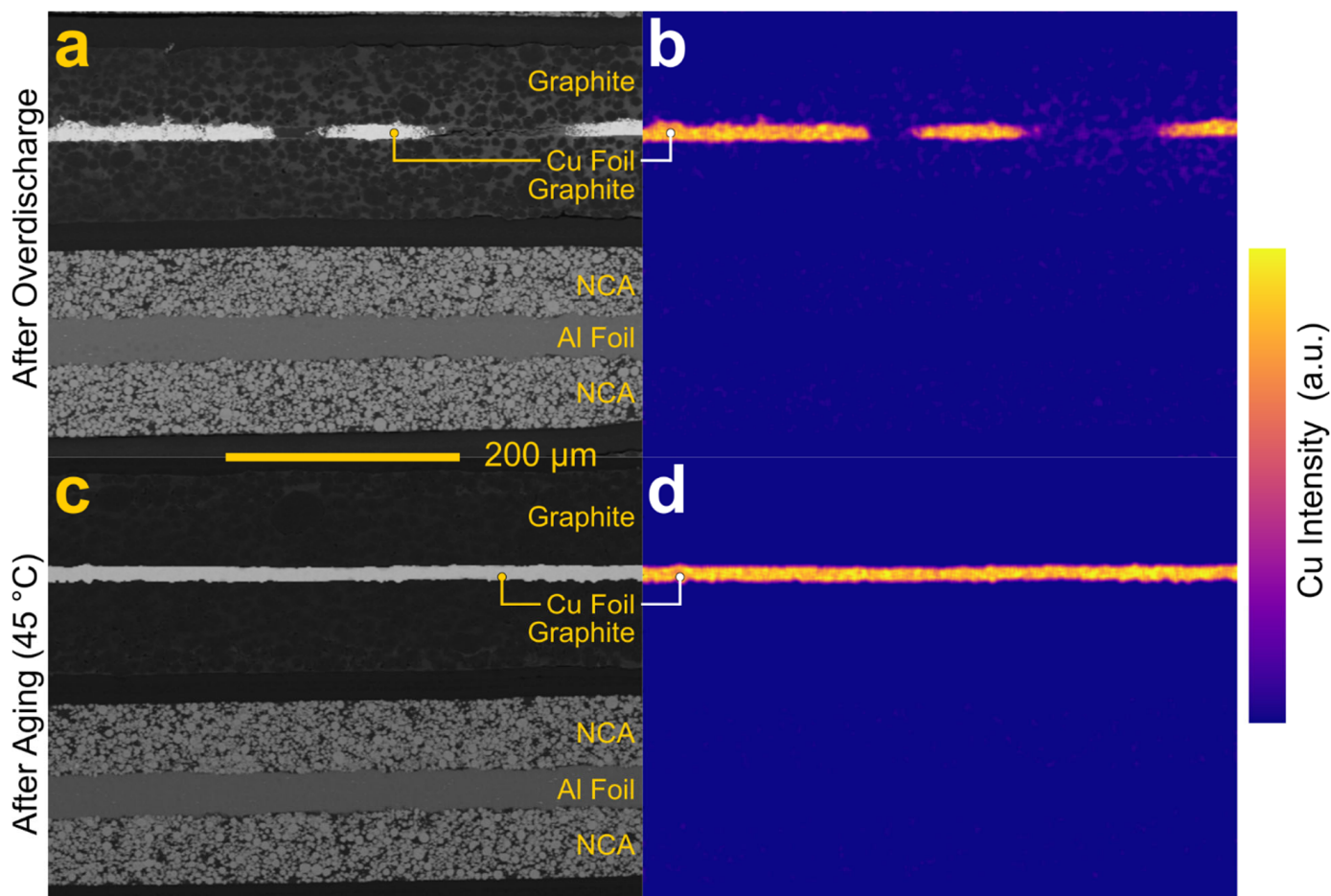
Figure 10. Backscatter (**a**,**c**) and Cu-K EDS map (**b**,**d**) of the overdischarged (**a**,**b**) and aged (**c**,**d**) graphite cells. The color indicates the Cu-K signal intensity. All images are scaled equally.

3.4. Analysis of Overdischarge Results

The baseline cycling results are consistent with the cell manufacturer's specification (where available) and reflect the behavior of cells that have not yet reached end-of-life (where accelerating capacity loss and/or growth in resistance are expected) [4–6,13]. This provides a reasonable foundation by which to compare the overdischarge performance.

Significant damage to the graphite cells is immediately apparent after the first overdischarge period. On cycle 49 (just prior to the first overdischarge), graphite cells from both groups (baseline and overdischarge) exhibited a discharge capacity of 99.5% of the original capacity. On cycle 51 (immediately following the first overdischarge), the capacity of the overdischarge cells dropped to 97.6–97.8% of the initial capacity. By cycle 99, this had fallen to 91.8–92.9% of the initial capacity. Each subsequent overdischarge further accelerated the rate of capacity loss.

Two primary reactions are of concern during the deep overdischarge of graphite-based Li-ion cells: solid electrolyte interphase (SEI) decomposition and the dissolution of the copper current collector. SEI decomposition occurs when the negative electrode potential rises above the stability window of the SEI. Once decomposed, a new layer of SEI will be spontaneously re-formed the next time the cell is recharged (when the negative electrode potential drops below the stability window of the electrolyte). This process damages the cell by (a) consuming the electrolyte (both solvent and salt), (b) generating gas within the cell, and (c) forming a new and less uniform layer of SEI. Notably, even with a trickle recharge at a low voltage, the SEI formation that occurs after deep overdischarge is not as controlled as that which occurs during the formation process during battery manufacturing. Many cell manufacturers include sacrificial additives that promote the formation of a stable

SEI; these additives are often fully consumed during the initial formation and would not be present during the reformation occurring after overdischarge [14]. The gas formed during SEI reformation is also trapped within the cell. For pouch cells, this may result in the cell swelling and, in extreme cases, a rupture of the pouch. For prismatic cells (like the cells investigated here), this gas increases the internal pressure and can result in the case bulging.

The SEI reformation process continues even after the first recharge. This is apparent here through the continued capacity loss during the 50 cycles between each overdischarge period (at a rate in excess of that observed in the baseline cycling). SEI formation is hypothesized to continue throughout a cell's life, but at a rate that slows with time [8,15,16]. By overdischarging and then continuing to cycle these cells, this process is restarted, resulting in accelerating damage to the cells.

In addition to SEI decomposition, copper dissolution is a concern for cells that are deeply overdischarged. Copper is universally used as the current collector for graphite negative electrodes because of its electrochemical stability at the necessary potentials. However, if the electrode potential rises above the stability window, the copper will dissolve into the electrolyte. This dissolved copper will redeposit (often in dendrite or cloud-like formations) upon subsequent recharge [17–19]. The copper dissolution potential is 3.38 V, vs. Li/Li$^+$ in a standard aqueous solution [20]. Despite this, we observed evidence of copper dissolution and replating in the post-overdischarge cross-section of these cells. This suggests that repeated and sustained discharging to 0 V (as may occur when a battery-containing device is left unused for an extended period) is sufficient to drive copper dissolution within a graphite-based lithium-ion battery.

Both SEI decomposition and copper dissolution are electrochemical processes, and the excess charge passed from the graphite cells at 0 V likely reflects the rate of reaction of both processes. We observed that the current decayed over the first several days of each overdischarge. This suggests that the SEI decomposition reaction may gradually decelerate before reaching a steady state. Subsequent overdischarges were found to exhibit progressively higher currents (especially in the latter days of each discharge), suggesting that the SEI decomposition reaction may be accelerated as a result of repeated overdischarges. In the final two overdischarge periods, the current at 0 V became increasingly erratic, which is consistent with the higher rates of pitting corrosion of the copper electrode [21].

No evidence of any detrimental impacts to the LTO cells was observed after multiple extended overdischarge periods, although the LTO electrodes have been shown to form SEI layers [1,2]. These cells also used an aluminum current collector and are, thus, not susceptible to copper dissolution. As a result, deeply discharging the LTO cells fully delithiated the LTO negative electrode and lithiated the positive electrode, both of which are stable in this state. Both LTO and cobalt oxide-based positive electrode materials have very steep voltage profile curves in this state, so relatively little current is passed during the overdischarge process. As with the graphite cells, the current at 0 V started out relatively high (close to the C/100 discharge rate) and declined as the electrodes become fully (de)lithiated. After this, the current reached a steady (slightly non-zero) value, resulting in a gradual increase in accumulated charge over the period of time at 0 V. The cause of this current is currently unexplained; however, it does not appear to result in any lasting damage to the cells.

3.5. Accelerated Aging at High SOC

Ordinary charge/discharge cycling serves as a useful way to accelerate the aging reactions in Li-ion batteries that occur during active use (especially during charge). However, this type of test does not capture the effect of calendar aging and/or the degradation that occurs chemically when cells are stored at a fixed SOC for extended periods. To examine this, we also performed thermally accelerated aging at a fixed SOC for both the LTO and graphite cells.

Figure 11 presents the change in several metrics over the course of aging at various temperatures for 135 days. The ells were stored at 100% of SOC at the specified temperature,

based on the standard charge condition for each cell. Voltage was monitored throughout aging and the cells were recharged when the OCV fell below the estimated 95% SOC voltage. Recharge frequency was found to decrease with aging; most cells were recharged at least once during the first aging period, while only two cells were recharged during the third aging period (50 days), and no cells were recharged while aging after the fourth aging period (64 days) was completed (see Appendix C and Figure A1).
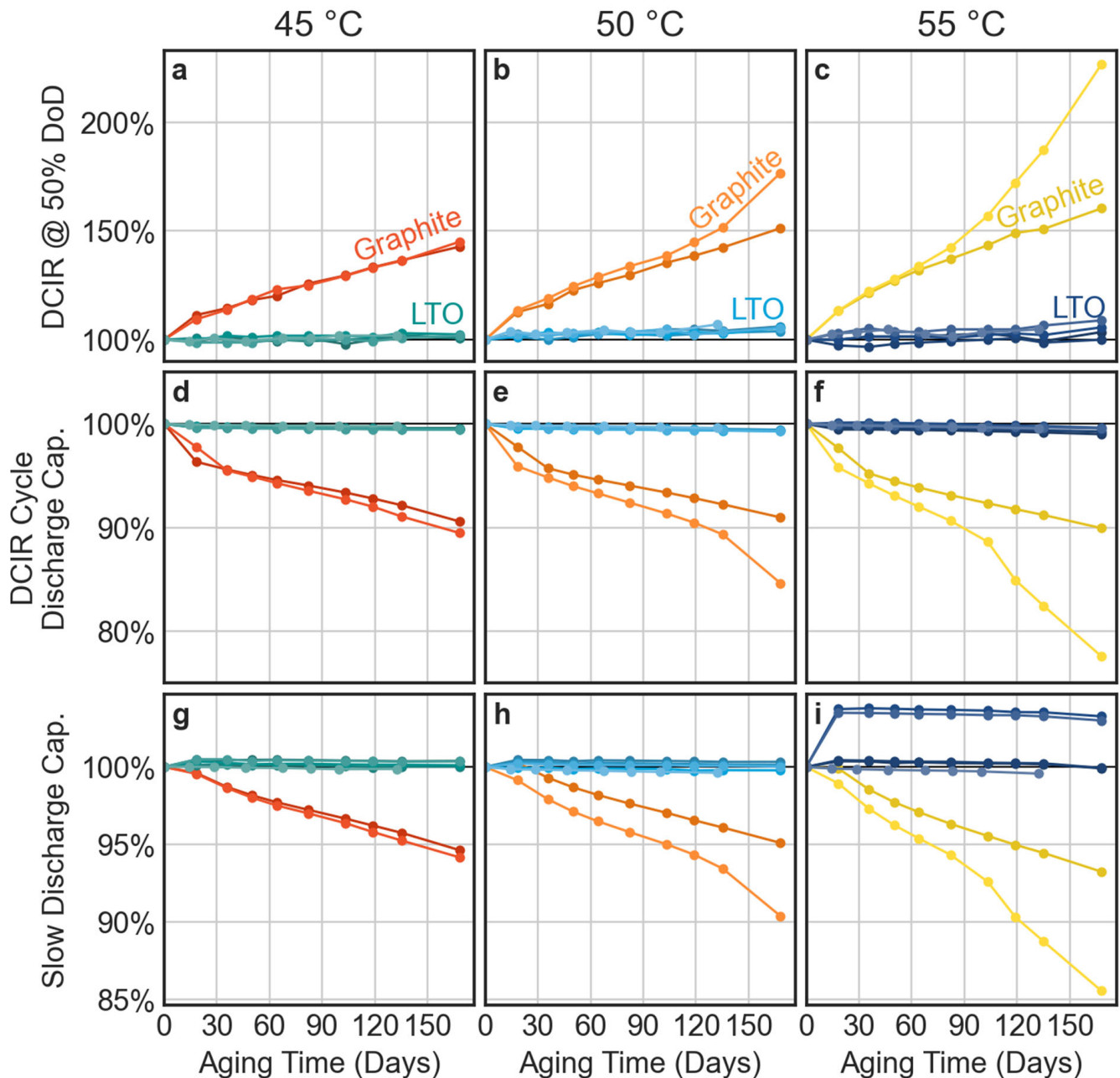
Figure 11. Change in various metrics vs. aging time at 45 °C (**a,d,g**), 50 °C (**b,e,h**), and 55 °C (**c,f,i**). All metrics were normalized relative to the pre-aging value of that metric. Top row (**a,b,c**) DCIR at 50% depth of discharge. Middle row (**d,e,f**) discharge capacity of the DCIR cycle. Bottom row (**g,h,i**) C/24 discharge capacity. The graphite cells are depicted in warm colors (red, orange, yellow) while the LTO cells are depicted in cool colors (teal, blue, navy).

Graphite cells exhibited significant changes in all three of the metrics investigated here (the DCIR at 50% DoD, the discharge capacity of the DCIR cycle, and the C/24 discharge

capacity) at all temperatures after the first aging period. These changes continued to grow along with additional aging, with an increase of more than 40% in DCIR and a loss of at least 4% of the initial capacity at both rates after 135 days of aging. One graphite cell that had been aged at 55 °C (shown in bright yellow in Figure 11) appeared to enter a second phase of reaction after ~100 days of aging, exhibiting an increased rate of capacity loss and DCIR growth after this point.

LTO cells exhibited no significant change in any of the metrics over the study period at any temperature. No cell exhibited more than a 1% loss in capacity after aging at any temperature, and the rise in DCIR was not more than 10% for all cells. A slight (<1%) variation in capacity was observed during the initial characterization cycle prior to aging (relative to subsequent cycles), which can be attributed to these cells still "breaking-in" after manufacturing. Additionally, two LTO cells that were later aged at 55 °C exhibited an anomalously low C/24 discharge capacity during the pre-aging characterization cycle.

3.6. Thermally Accelerated Aging and Predictions

Aging the cells at various temperatures and measuring their performance enabled a predictive model to be built that reflects the long-term aging expected to occur in these cells at normal operating temperatures. This is performed using a modified version of the Arrhenius equation, shown in Equation (1) below:

$$\Delta M = k \cdot bt^x = Ae^{-\frac{E_A}{RT}} \cdot t^x = e^{C - \frac{E_A}{RT}} \cdot t^x \tag{1}$$

This formula states that the change in a measurable cell property (such as discharge capacity or DCIR) is proportional to the reaction rate constant k and a power-law time-dependence. The choice of a power-law time-dependent relationship is arbitrary but is well justified in practice, as it can describe a range of reaction regimes (both accelerating and decelerating) with a single variable. In addition, the growth of a passivating layer on a surface is theoretically described by $t^{1/2}$, and this has been used to model the rate of SEI growth and DCIR [6–8,22,23]. The reaction rate constant, k, can be substituted with the right-hand side of the Arrhenius equation to produce an explicit temperature component to the formula, which is controlled by the activation energy, E_A. This results in a formula where the change in a given metric (ΔM) is dependent on two experimental conditions (time, t, and the absolute aging temperature, T), the ideal gas law constant, R, and three empirically derived parameters: the prefactor A (or the prefactor exponential, C), the activation energy, E_A, and the time-dependent power-law factor, x. In addition to the assumption about time dependence, this model also assumes that the measured change in performance is controlled by the same reaction mechanism in all cells and at all temperatures. Heating cells to too high a temperature can defeat this assumption, resulting in poor model fits and/or necessitating the exclusion of that data. For this reason, the maximum temperature for this study was limited to 55 °C.

With this formula, we used all the collected aging data for a particular cell type and metric and produced a model that relies on only three adjustable parameters. For each metric of interest, the change in the metric was calculated with the formula $\Delta M = 1 - \frac{M}{M_0}$ or $\Delta M = \frac{M}{M_0} - 1$ (depending on the expected direction of the expected change in the metric). This value, along with the total aging time and absolute aging temperature, was then fitted against Equation (1), as defined above, to solve it for C, E_A, and x. The details of this fitting process are described in Appendix D.

Figure 12 presents multiple ways of evaluating the quality of fit of the rise in DCIR at 50% DoD, in both the graphite and LTO cells. For the graphite cells, this metric fitted well with the modified Arrhenius model, with a predicted vs. actual R^2 value of 98%. In contrast, the LTO cells were not a good fit for this metric, with an R^2 value of just 19%. Both groups shared similar root mean squared errors (graphite: 0.018, LTO: 0.019), which indicated that the poor LTO fit was due to the lack of signal. As can be seen in the top row of Figure 11 (showing the raw aging data for these values), the LTO cells exhibited very

little systematic change in this metric over the study period. Similar data for the DCIR cycle discharge capacity are presented in Appendix E and Figure A2.
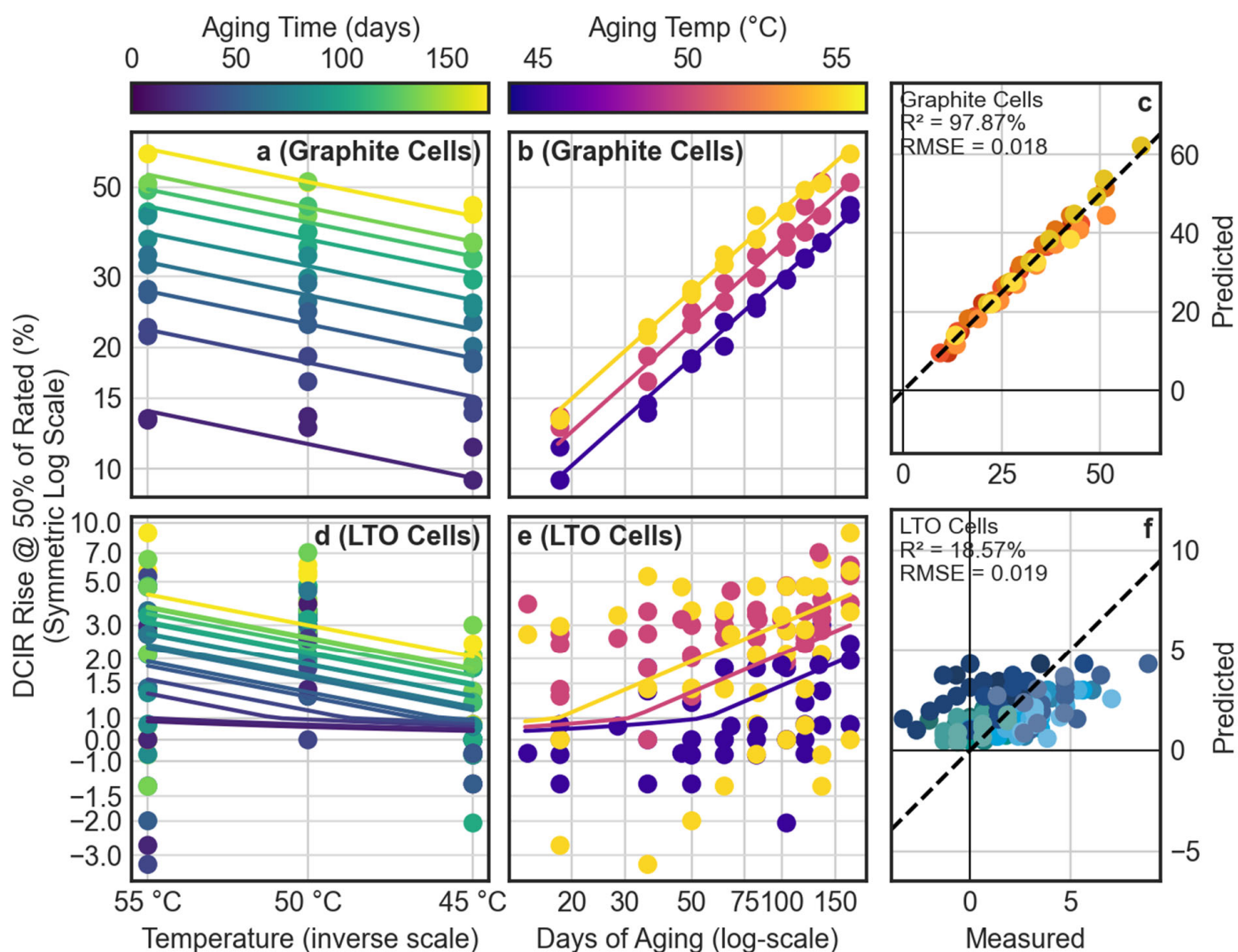
Figure 12. Quality of fit metrics for the modified Arrhenius fit of the DCIR at 50%. Upper plots (**a–c**): the graphite cells. Lower plots (**d–f**): the LTO cells. Left column (**a,d**): the rise in DCIR (symmetric log scale) vs. aging temperature (plotted on an inverse absolute temperature scale), with colors indicating aging time. Middle column (**b,e**): the rise in DCIR vs. aging time, with colors indicating aging temperature. The points indicate measured data, while the lines reflect the best fit for the model. Right column (**c,f**): the predicted vs. the actual results. Colors reflect the individual cells; the 45° line indicates a perfect agreement between the model and the data.

Figure 13 shows the aging data and model predictions at the various aging temperatures for DCIR at 50% DoD and the DCIR cycle discharge capacity. For both metrics, the graphite cell model parameters fitted the data reasonably well (R^2 = 89% and 79%, respectively). In contrast, the LTO cells were not predicted well, as the change in these metrics is small, relative to the measurement error. For the graphite cells, the DCIR at 50% DoD was predicted to have a power-law dependence of 0.67 (95% confidence interval (CI): 0.64–0.71) and an activation energy of 33.2 kJ/mol (95% CI: 29.8–36.7 kJ/mol). The higher-than-expected time dependence suggests that the processes affecting this metric are not following a theoretical film passivation reaction scheme. The DCIR cycle discharge capacity loss was predicted to follow a square root time-dependence (x = 0.48; 95% CI: 0.42–0.55) with a significantly lower activation energy (13.1 kJ/mol; 95% CI: 4.8–21.8 kJ/mol). The

LTO cells exhibited very slight changes in DCIR (<5%) and DCIR discharge capacity (<1%) in all conditions. Because of this, the confidence intervals on the fits for these parameters are extremely wide. Additional aging (possibly at higher temperatures) is required to increase confidence in these parameters [24].
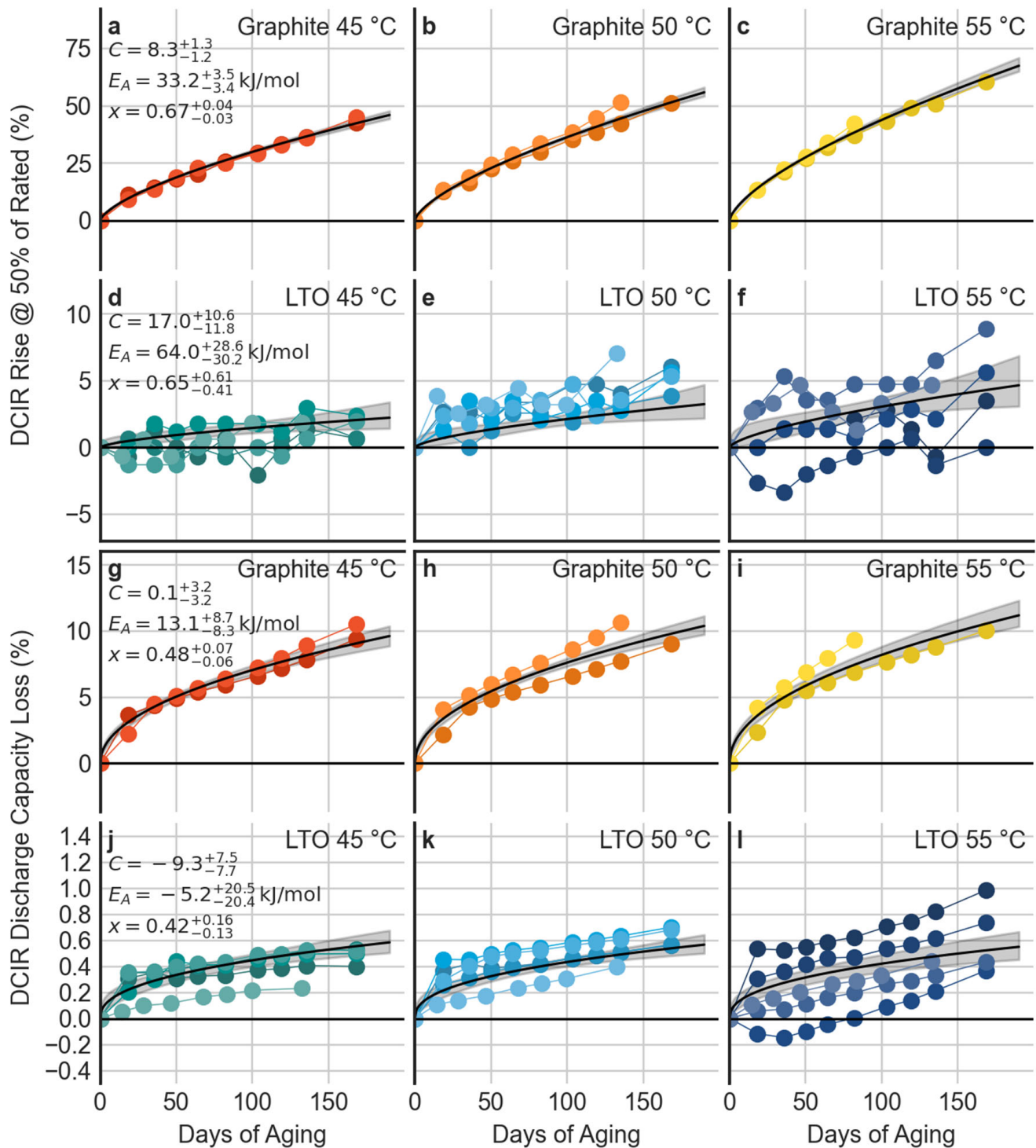
Figure 13. Aging data and modeled predictions. For all plots, colored dots and lines reflect the measured data, while the solid black curves reflect the model prediction. Shaded regions reflect the 95% confidence interval for the population average. Fit parameters are shown on the left-most plot in each row. Top two rows (**a**–**f**) the rise in DCIR at 50% DoD. Bottom two rows (**g**–**l**) the C/24 discharge capacity.

Finally, the long-term predictions at 37 °C are shown in Figure 14. Based on these models, the graphite cell population is expected to experience significant aging after 5 years of storage at 100% SOC in a 37 °C environment, with the internal resistance increasing by 2.5× and the DCIR cycle discharge capacity dropping by 30% (only the population average is predicted; confidence intervals for individual cells are not predicted). In contrast, the LTO cells are expected to see a less than 30% increase in DCIR over this period (based on the upper boundary of the 95% CI). It is important to note that the extrapolated predictions here should be viewed as optimistic; these predictions assume that the reactions observed to date will continue to develop at the same rate. Additional reactions that have not been accounted for in the model (such as electrolyte depletion) are generally expected to accelerate the rate of aging above those figures predicted here.
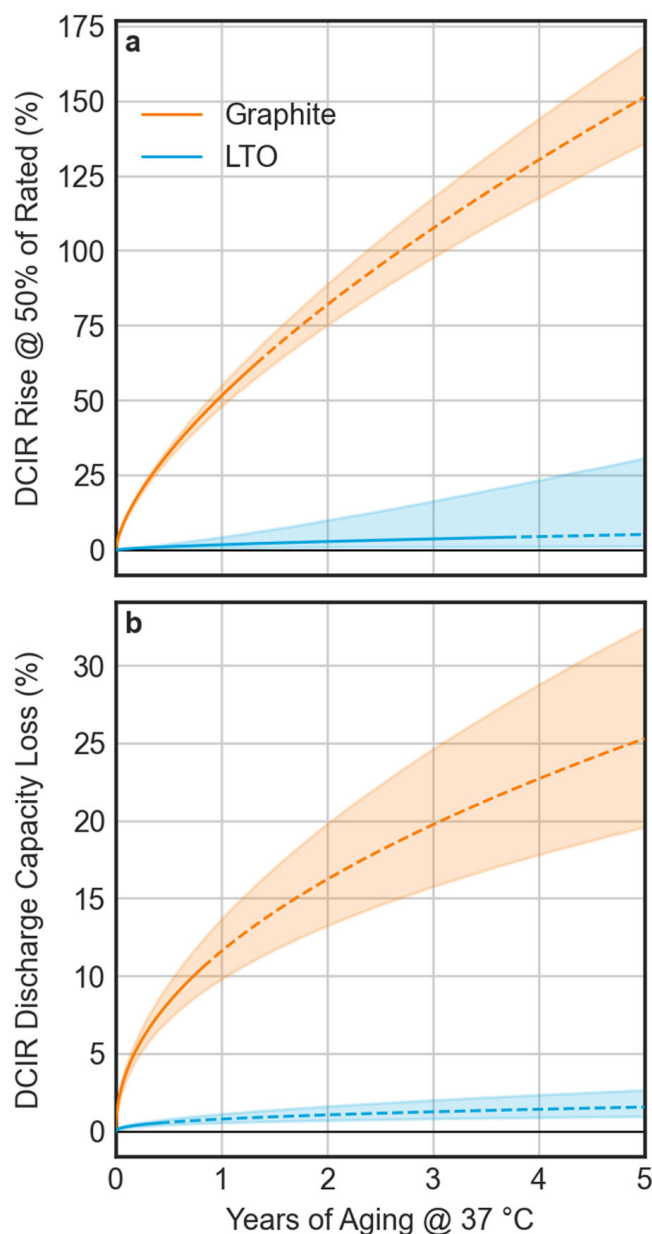
Figure 14. Long-term aging prediction at 37 °C. Solid lines represent the prediction within the range of aging observed in the accelerated aging test. Dotted lines reflect the extrapolated performance beyond this point. Shaded regions reflect the 95% confidence interval for the population mean. (**a**) The predicted rise in DCIR @ 50% SOC; (**b**) the predicted DCIR discharge capacity loss.

4. Discussion and Conclusions

In this work, we explored the performance of two different commercial lithium-ion batteries intended for use in implanted medical applications; one used a traditional graphite electrode and the other, a lithium titanium oxide (LTO) negative electrode. We investigated their response to two different aging scenarios (deep overdischarge and extended storage at high states of charge). During overdischarge, the graphite-based cells were found to exhibit signs of significant degradation after one 7-day overdischarge period at 0 V, and the degradation accelerated with each subsequent overdischarge session. We identified behaviors consistent with SEI degradation during overdischarge and reformation on subsequent recharge, as well as signs of copper dissolution and replating. Using thermally accelerated static aging at 100% state-of-charge, we observed that the graphite-based cells aged significantly when stored at temperatures of between 45 °C and 55 °C for approximately 4 months, allowing the development of a robust model to predict long-term changes in internal resistance (DCIR) and capacity loss. The LTO-based cells exhibited minimal aging under the same conditions, which limited the precision of the model. Despite this, the very small amount of aging observed suggests that these cells will exhibit excellent long-term (>5 years) performance, even when stored at 37 °C.

Appendix A

DC internal resistance (DCIR) values in this article are derived from the voltage recovery that occurs during the first 60 s of each rest during the DCIR discharge cycle. The DCIR is calculated using the following formula:

$$\text{DCIR} = \frac{\Delta V}{\Delta I} = \frac{V_2 - V_1}{I_{disch} - 0} \tag{A1}$$

where V_1 is the final voltage measured prior to the start of the rest, V_2 is the voltage measured 60 s after the start of the rest, and I_{disch} is the discharge current (0.5C). This value was calculated for each DCIR rest pulse (every 10% of the SOC) during each DCIR cycle for all cells.

Appendix B

Differential capacity (dQ/dV) was calculated using the following algorithm:

1. Group the measurements sequentially, such that all points within each group have a voltage close to one another (where closeness is an adjustable parameter).
2. For each group, calculate the mean voltage and capacity.
3. Then, calculate the change in voltage and capacity between each group in order.
4. The differential capacity is calculated by dividing the change in capacity by the change in voltage for each group.

The closeness parameter was tuned to be as small as possible while minimizing sign reversals at voltage plateaus (which occur when random fluctuations in the voltage exceed the closeness threshold). A closeness limit of 3 mV was found to be optimal, which is close to the voltage accuracy of the battery cyclers (2 mV).

Appendix C

The number of recharges that occurred during aging between the characterization timepoints is shown in Figure A1. Most aging periods were approximately 14 days long.
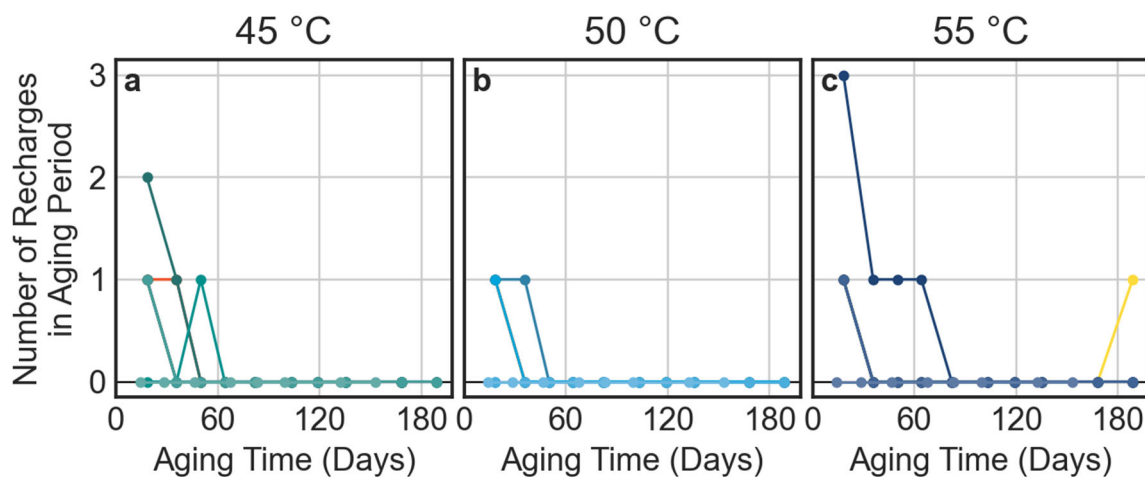

Figure A1. The number of recharges that occurred during each aging period.

Appendix D

Equation (1) can be linearized by taking the natural log of both sides, which is shown here as Equation (A2):

$$\ln(\Delta M) = C - \frac{E_A}{R} \cdot \frac{1}{T} + x \cdot \ln(t) \tag{A2}$$

In this form, $\ln(\Delta M)$ is linear with respect to $\frac{1}{T}$ and $\ln(t)$, and can be solved using an ordinary least squares (OLS) solver. While this produces a useful analytical relationship, fitting directly to Equation (A2) requires the rejecting of all data where ΔM is nonpositive, and this formula increases the weight of very small values of ΔM. Therefore, the final fit optimization is performed using a nonlinear minimizer on the exponential form of Equation (1).

The algorithm used to calculate the best fit for the parameters is as follows:

1. Collect all aging measurements (at all temperatures) for a given cell type; remove any rejected data points.
2. Calculate ΔM for each measurement.
3. Calculate the preliminary values of C, E_A, and x, using Equation (2) and an OLS solver with reasonable bounds (stated below), for all three parameters
4. Calculate the final values of C, E_A, and x, using Equation (1) and an initial guess taken from the solution found in step 2.

For this analysis, the following boundaries were used: $-50 \leq C \leq 50$, $-100 \frac{kJ}{mol} \leq E_A \leq 100 \frac{kJ}{mol}$ and $0.01 \leq x \leq 3$. For E_A and x, these boundaries are significantly wider than the expected range of reasonable outcomes; solutions found near the extremes of the boundaries were interpreted to indicate a poor-quality prediction. The boundaries for C were chosen to prevent numerical errors during the evaluation of Equation (1).

Bootstrapping was used to estimate the confidence interval of each of the parameters. For each fit, 10,000 iterations of steps (3) and (4) above were repeated on random samples. The percentile method was used to estimate the confidence intervals for each parameter, as it has been reported that this is more accurate when including the underlying statistic than alternative methods [25].

Predictions were made by taking the fitted parameters and entering them into Equation (1), along with the desired time and temperature of the prediction. Confidence intervals were estimated by evaluating each of the bootstrapped solutions at the given time/temperature. The percentile method was then used to estimate the upper and lower boundaries on the confidence interval for each unique time/temperature combination.

Appendix E

The quality-of-fit metrics for the DCIR discharge capacity are presented in Figure A2. All panels have the same meaning as those described in Figure 12.
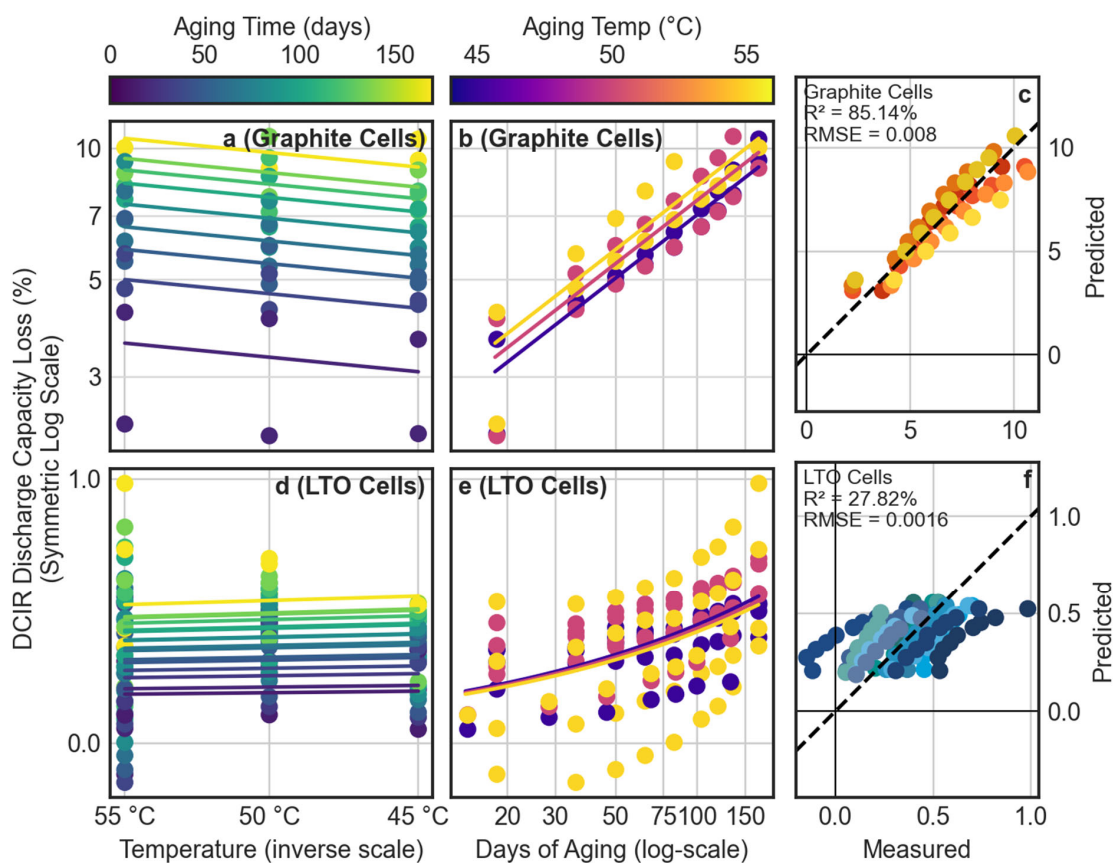
Figure A2. Quality of fit metrics for the modified Arrhenius fit of the DCIR cycle discharge capacity. Upper plots (**a**–**c**): the graphite cells. Lower plots (**d**–**f**): the LTO cells. Left column (**a**,**d**): capacity loss (symmetric log scale) vs. aging temperature (plotted on an inverse absolute temperature scale), with colors indicating aging time. Middle column (**b**,**e**): capacity loss vs. aging time, with colors indicating the aging temperature. Points indicate the measured data, lines reflect the best fit for the model. Right column (**c**,**f**): predicted vs. actual figures. Colors reflect individual cells; the 45° line indicates a perfect agreement between the model and the data.

References

1. He, Y.-B.; Liu, M.; Huang, Z.-D.; Zhang, B.; Yu, Y.; Li, B.; Kang, F.; Kim, J.-K. Effect of Solid Electrolyte Interface (SEI) Film on Cyclic Performance of Li$_4$Ti$_5$O$_{12}$ Anodes for Li Ion Batteries. *J. Power Sources* **2013**, *239*, 269–276. [CrossRef]
2. Gauthier, N.; Courrèges, C.; Demeaux, J.; Tessier, C.; Martinez, H. Probing the In-Depth Distribution of Organic/Inorganic Molecular Species within the SEI of LTO/NMC and LTO/LMO Batteries: A Complementary ToF-SIMS and XPS Study. *Appl. Surf. Sci.* **2020**, *501*, 144266. [CrossRef]
3. Brunell, M. Modelling and Predictive Performance of Lithium Titanate. Ph.D. Thesis, University of Warwick, Coventry, UK, 2020.
4. Atalay, S.; Sheikh, M.; Mariani, A.; Merla, Y.; Bower, E.; Widanage, W.D. Theory of Battery Ageing in a Lithium-Ion Battery: Capacity Fade, Nonlinear Ageing and Lifetime Prediction. *J. Power Sources* **2020**, *478*, 229026. [CrossRef]
5. Su, L.; Zhang, J.; Wang, C.; Zhang, Y.; Li, Z.; Song, Y.; Jin, T.; Ma, Z. Identifying Main Factors of Capacity Fading in Lithium Ion Cells Using Orthogonal Design of Experiments. *Appl. Energy* **2016**, *163*, 201–210. [CrossRef]
6. Spotnitz, R. Simulation of Capacity Fade in Lithium-Ion Batteries. *J. Power Sources* **2003**, *113*, 72–80. [CrossRef]
7. Fathi, R.; Burns, J.C.; Stevens, D.A.; Ye, H.; Hu, C.; Jain, G.; Scott, E.; Schmidt, C.; Dahn, J.R. Ultra High-Precision Studies of Degradation Mechanisms in Aged LiCoO$_2$/Graphite Li-Ion Cells. *J. Electrochem. Soc.* **2014**, *161*, A1572. [CrossRef]
8. Smith, A.J.; Burns, J.C.; Zhao, X.; Xiong, D.; Dahn, J.R. A High Precision Coulometry Study of the SEI Growth in Li/Graphite Cells. *J. Electrochem. Soc.* **2011**, *158*, A447. [CrossRef]
9. Cai, C.; Nie, Z.; Robinson, J.P.; Hussey, D.S.; LaManna, J.M.; Jacobson, D.L.; Koenig, G.M. Thick Sintered Electrode Lithium-Ion Battery Discharge Simulations: Incorporating Lithiation-Dependent Electronic Conductivity and Lithiation Gradient Due to Charge Cycle. *J. Electrochem. Soc.* **2020**, *167*, 140542. [CrossRef] [PubMed]
10. Wang, B.; Bates, J.B.; Hart, F.X.; Sales, B.C.; Zuhr, R.A.; Robertson, J.D. Characterization of Thin-Film Rechargeable Lithium Batteries with Lithium Cobalt Oxide Cathodes. *J. Electrochem. Soc.* **1996**, *143*, 3203. [CrossRef]
11. Li, J.; Harlow, J.; Stakheiko, N.; Zhang, N.; Paulsen, J.; Dahn, J. Dependence of Cell Failure on Cut-Off Voltage Ranges and Observation of Kinetic Hindrance in LiNi$_{0.8}$Co$_{0.15}$Al$_{0.05}$O$_2$. *J. Electrochem. Soc.* **2018**, *165*, A2682. [CrossRef]
12. Jmol: An Open-Source Java Viewer for Chemical Structures in 3D. Available online: http://jmol.sourceforge.net/ (accessed on 17 November 2021).
13. Wright, R.B.; Christophersen, J.P.; Motloch, C.G.; Belt, J.R.; Ho, C.D.; Battaglia, V.S.; Barnes, J.A.; Duong, T.Q.; Sutula, R.A. Power Fade and Capacity Fade Resulting from Cycle-Life Testing of Advanced Technology Development Program Lithium-Ion Batteries. *J. Power Sources* **2003**, *119–121*, 865–869. [CrossRef]
14. Kim, K.; Ma, H.; Park, S.; Choi, N.-S. Electrolyte-Additive-Driven Interfacial Engineering for High-Capacity Electrodes in Lithium-Ion Batteries: Promise and Challenges. *ACS Energy Lett.* **2020**, *5*, 1537–1553. [CrossRef]
15. Liu, L.; Park, J.; Lin, X.; Sastry, A.M.; Lu, W. A Thermal-Electrochemical Model That Gives Spatial-Dependent Growth of Solid Electrolyte Interphase in a Li-Ion Battery. *J. Power Sources* **2014**, *268*, 482–490. [CrossRef]
16. Wang, A.; Kadam, S.; Li, H.; Shi, S.; Qi, Y. Review on Modeling of the Anode Solid Electrolyte Interphase (SEI) for Lithium-Ion Batteries. *NPJ Comput. Mater.* **2018**, *4*, 1–26. [CrossRef]
17. Guo, R.; Lu, L.; Ouyang, M.; Feng, X. Mechanism of the Entire Overdischarge Process and Overdischarge-Induced Internal Short Circuit in Lithium-Ion Batteries. *Sci. Rep.* **2016**, *6*, 30248. [CrossRef]
18. Ouyang, D.; Chen, M.; Liu, J.; Wei, R.; Weng, J.; Wang, J. Investigation of a Commercial Lithium-Ion Battery under Overcharge/over-Discharge Failure Conditions. *RSC Adv.* **2018**, *8*, 33414–33424. [CrossRef]
19. Chen, C.; He, G.; Cai, J.; Zhao, Z.; Luo, D. Investigating the Overdischarge Failure on Copper Dendritic Phenomenon of Lithium Ion Batteries in Portable Electronics. In Proceedings of the 2019 22nd European Microelectronics and Packaging Conference Exhibition (EMPC), Pisa, Italy, 16–19 September 2019; pp. 1–6.
20. Vanýsek, P. *Electrochemical Series*; Haynes, W.M., Lide, D.R., Eds.; CRC Press; Taylor and Francis: Boca Raton, FL, USA, 2010; pp. 8.20–8.29.
21. Heusler, K.E. Growth and Dissolution of Passivating Films. *Corros. Sci.* **1990**, *31*, 597–606. [CrossRef]
22. Tang, M.; Lu, S.; Newman, J. Experimental and Theoretical Investigation of Solid-Electrolyte-Interphase Formation Mechanisms on Glassy Carbon. *J. Electrochem. Soc.* **2012**, *159*, A1775. [CrossRef]
23. Ploehn, H.J.; Ramadass, P.; White, R.E. Solvent Diffusion Model for Aging of Lithium-Ion Battery Cells. *J. Electrochem. Soc.* **2004**, *151*, A456. [CrossRef]
24. Ye, H.; Jain, G. Rechargeable Lithium Ion Batteries for Implantable Neurostimulators. In Proceedings of the International Battery Seminar, Fort Lauderdale, FL, USA, 25–28 March 2019.
25. Jung, K.; Lee, J.; Gupta, V.; Cho, G. Comparison of Bootstrap Confidence Interval Methods for GSCA Using a Monte Carlo Simulation. *Front. Psychol.* **2019**, *10*, 2215. [CrossRef] [PubMed]